Sustainable Energy & Fuels

ROYAL SOCIETY OF CHEMISTRY

PAPER

View Article Online
View Journal | View Issue

Cite this: *Sustainable Energy Fuels*, 2025, **9**, 5057

Enhancing thermal comfort and photovoltaic efficiency through thermotropic starch–hydrogel composite membrane integration in sustainable building fenestration

Anurag Roy, *[a] Adeel Arshad, [ab] Tapas Kumar Mallick [ac] and Asif Ali Tahir *[a]

This study develops a transparent, biocompatible hydrogel membrane (HGM) for sustainable building fenestration. Made from hydroxypropyl cellulose, poly(acrylic acid), and starch derived from waste potato peels, the HGM leverages bio-waste valorization. It exhibits thermotropic behavior, dynamically adjusting optical transparency with temperature. Extensive physicochemical analyses confirmed the molecular interactions governing its optical and thermal properties. When incorporated into a prototype double-glazed window, the HGM significantly enhanced indoor thermal regulation, achieving a low thermal conductivity at 0.23 W m^{-1} K^{-1} and thermal transmittance (*U*-value) of 1.84 W m^{-2} K^{-1} and effectively mitigating temperature differentials of up to 30 °C. The synthesized hydrogel exhibits a tunable transition temperature, high luminous transmittance of 72%, notable solar modulation efficiency of 75%, and exceptional durability. In addition to thermal performance, the HGM improved the efficiency of the underlying silicon photovoltaic cell by up to 15% compared with its standalone performance. This enhancement is attributed to the presence of light-scattering centers within the HGM, which facilitate total internal reflection and contribute to thermal buffering. Functioning dually as a passive radiative cooling layer and an optical modulator, the HGM material demonstrates multifunctionality tailored for building-integrated photovoltaic systems. This study advances the domain of energy-efficient architecture by integrating sustainable materials with improved solar and thermal regulation properties, thereby promoting the development of climate-responsive building designs.

Received 26th January 2025
Accepted 23rd July 2025

DOI: 10.1039/d5se00124b

rsc.li/sustainable-energy

1. Introduction

Growing apprehensions regarding global energy consumption and the escalating carbon footprint have shifted the policy focus towards buildings. Buildings currently account for 40% of the world's total energy consumption and generate 15% of global carbon dioxide emissions.[1,2] However, the limited thermal insulation properties and high solar radiation transmittance of glazed facades substantially contribute to increased building energy demand. Statistical analyses reveal that glazed façades are responsible for approximately 37% of total solar heat gain and 40% of the overall heat loss through building envelopes.[3] A significant contributing factor to this scenario lies in the systems employed to maintain thermal and visual comfort within buildings, notably air conditioning and heating, representing primary energy consumers. Consequently, optimizing these systems has become imperative. It is noteworthy that although windows typically constitute only about 30% of a building's external facade, they contribute to approximately 60% of its energy loss. While their primary function of a window is to illuminate the interior by permitting visible light, they also play a pivotal role in regulating thermal comfort levels within the building.[4,5] This dual functionality underscores the importance of designing windows that balance energy efficiency and visual comfort. Smart materials integrated into window systems—often referred to as intelligent glazing technologies, exhibit dynamic physicochemical responses to environmental stimuli such as temperature and light, thereby improving building energy efficiency and occupant comfort.[6] Most existing smart materials in windows employed in building envelopes are predominantly synthetic oxide-based nanomaterials, which often exhibit a high transition temperature and elevated thermal conductivity that compromises optical transparency, thereby limiting their effectiveness in optimizing energy performance.[7,8] The incorporation of sustainable, biocompatible materials into adaptive building systems thus represents a largely untapped opportunity. Furthermore, current

[a]*Solar Energy Research Group, Department of Engineering, Environmental and Sustainability Institute, University of Exeter, Penryn Campus, Cornwall TR10 9FE, UK. E-mail: a.roy30@exeter.ac.uk; a.tahir@exeter.ac.uk*

[b]*Department of Mechatronics and Biomedical Engineering, College of Engineering and Physical Sciences, Aston University, Birmingham B4 7ET, UK*

[c]*Department of Mechanical and Energy Engineering, College of Engineering, Imam Abdulrahman Bin Faisal University, Saudi Arabia*

technologies frequently lack a comprehensive integration of thermal comfort and energy generation functionalities. Research into organic, bio-based or bio-influenced materials for responsive architectural applications remains scarce, despite the growing imperative for sustainability.[9] Additionally, green building envelopes have already demonstrated their efficacy as thermal insulators, acoustic dampeners, and passive energy-saving components, collectively contributing to enhanced building sustainability metrics.[10]

Interestingly, lower critical solution temperature (LCST) type thermosensitive polymer-based hydrogels and liquids have garnered considerable interest owing to their cost-effectiveness, high solar modulation efficiency, superior luminous transmittance, and easily tunable phase transition temperatures.[11] The fundamental mechanism underlying their behaviour involves temperature-induced phase separation of the polymers in aqueous media. Below the cloud point, these polymers remain fully soluble, maintaining the hydrogel or liquid in a transparent state. Upon exceeding this critical temperature, polymer chains aggregate, leading to phase heterogeneity that scatters incident light and imparts a turbid or opaque appearance.[12] This reversible optical switching underpins their utility in smart window applications and other stimuli-responsive systems. Hydrogels have garnered significant attention in this context due to their highly tunable chemical and physical properties. Composed of three-dimensional networks of hydrophilic polymer chains, these materials are capable of swelling in water.[13] Particularly noteworthy are hydrogels derived from LCST-type thermosensitive polymers, which exhibit a distinct temperature-responsive behaviour.[14,15]

Recently, thermochromic hydrogels, exhibiting temperature-dependent optical transitions, have attracted significant interest for energy-efficient smart window applications. Notable examples include polyampholyte hydrogels (PAH), poly(*N*-isopropylacrylamide) (PNIPAM), and hydroxypropyl cellulose (HPC), each demonstrating phase transitions conducive to dynamic light modulation.[13,16,17] Hydrogels also offer revolutionary potential as high thermal energy storage (TES) materials for thermo-responsive smart windows, leveraging the intrinsic high solar modulation and TES capacity of water-rich thermoresponsive liquids. Unlike conventional building materials such as wood, metal, glass, and concrete, which have low TES capacities (<100 kJ kg^{-1} over 10–70 °C), hydrogels benefit from water's exceptional specific heat capacity (4.2 kJ kg^{-1} K^{-1}), yielding TES capabilities around 250 kJ kg^{-1}.[18,19] While commercial phase change materials like paraffin and fatty acids offer TES, their lack of optical transparency limits their suitability for glazing applications.

The adaptive "smart" behaviour of hydrogels allows dynamic modulation of transparency in response to outdoor temperature variations, optimizing visible light transmittance while maintaining superior indoor thermal comfort across varying climates.

Poly(*N*-isopropylacrylamide) (PNIPAM) hydrogel-based smart windows have achieved an outstanding intrinsic transmittance of 87.2%. When compared to commercially available glazing systems with a low-emissivity (low-e) coating, the PNIPAM–AEMA hydrogel film exhibits a combination of advantageous features including dynamic solar modulation and near-infrared (NIR) blocking.[20] This renders the adaptive dynamically controlled window particularly suitable for tropical regions. The PNIPAM network demonstrates an ultra-fast thermal response rate, alongside commendable thermochromic performances and anti-freezing properties, thereby facilitating effective indoor thermal control. Additionally, PNIPAM, akin to wood, exhibits robust mechanical properties, enhancing its optical regulation capabilities.[8] By incorporating this hydrogel into transparent wood, indoor air temperature can be reduced by 4.3 °C. The PNIPAM–polyacrylamide hydrogel is introduced as a robust gel exhibiting notable thermochromic properties. The incorporation of nanoparticles significantly enhances the photothermal conversion capabilities of the hydrogel. This advanced material allows the window to achieve approximately 80% visible light transmittance prior to activation, and effectively blocks around 90% of sunlight upon activation, making it highly efficient for adaptive light and heat regulation.[21] Chen *et al.* recently reported a poly(vinyl alcohol)–borax cross-linked hydrogel with 71.2% luminous transmittance, 72.2% solar modulation efficiency, and excellent durability. Compared to air-sandwiched windows, it offers superior cooling, with up to 50% temperature-responsive contribution, significantly influenced by hydrogel thickness, making it ideal for smart thermochromic window applications.[22]

As an alternative, cheaper cellulose derivatives, namely methylcellulose, hydroxypropyl cellulose (HPC), and hydroxypropyl methylcellulose, are widely acknowledged for their manifestation of LCST in aqueous environments. This phase transition primarily stems from the transition of different hydrogen bonds (H-bonds).[23,24] Furthermore, modulation of the phase transition temperature is achievable through adjustments in both the degree of substitution and molecular weight. Notably, metal ions exhibit robust hydration, thereby attenuating the polymer–water H-bond. Consequently, the LCST phase transition temperature is diminished in aqueous solutions containing metal ions. Concurrently, investigations into LCST-type hydrogels derived from sustainable cellulose sources have been conducted. Additionally, the inherent rigidity of cellulose facilitates the fabrication of mechanically robust hydrogels.[25,26] Recently, Mohammad *et al.* conducted control experiments that demonstrated the effectiveness of cellulose windows in providing heat shielding. Their findings revealed that methylcellulose-based hydrogel windows reduced indoor room temperatures by up to 39 °C, with a heating rate that was twofold lower compared to standard double-pane windows.[27]

Unlike liquid hydrogels, hydrogel membranes (HGMs) form stable, solid-like networks that eliminate the risks of leakage, evaporation, and structural failure, require no maintenance cost, and are easy to retrofit, enhancing long-term durability and safety. In this work, their thermo-responsive behaviour has been explored which allows them to dynamically switch between transparent and translucent states in response to temperature, enabling passive regulation of light and heat without any external energy input. Composed of water-based or

biocompatible materials such as starch or polyacrylic acid, HGMs are non-toxic, recyclable, and often biodegradable, aligning with green building practices and reducing their environmental impact.[28] Their thermo-responsive behaviour allows them to dynamically switch between transparent and translucent states in response to temperature, enabling passive regulation of light and heat without external energy input. This phase transition creates light-scattering centres that enhance diffuse light transmission and significantly boost photovoltaic (PV) performance through total internal reflection and improved photon capture.[29] Due to their solid-state, flexible structure, HGMs can be easily integrated into existing window assemblies without the need for complex sealing, fluid reservoirs, or pressure management systems typically required for liquids. This makes them ideal for cost-effective retrofitting in older buildings, where minimal structural modification is preferred. Their lightweight nature and ease of handling further simplify installation, reducing labour and material costs. In contrast, liquid systems often involve intricate containment setups and pose higher risks of leakage over time, making retrofitting more technically demanding and less reliable. Furthermore, their production typically involves lower embodied energy compared to more complex electrochromic or liquid systems. Collectively, these properties make HGMs a robust and sustainable solution for energy-efficient, smart window technologies in the modern built environment.

2. Materials and method

2.1 Materials

Fresh potatoes were procured from a local supermarket in Falmouth, Cornwall, UK, and utilized in their original state for extracting starch. Hydroxypropyl cellulose (HPC) with a molecular weight (MW) of 10 000, sourced from Merck GB, and polyacrylic acid (PAA) with a MW of 3000, also obtained from Merck GB, were employed. Glycerol and acetic acid were purchased from Fisher Scientific, UK, and utilized without additional purification steps. All solvents and chemicals used in the present work were analytical grade (E. Merck and BDH).

2.2 Extracting starch from potato waste peel

Potato peel waste (PPW) represents a biowaste stream often perceived as having negligible value, leading to its disposal with significant environmental implications, with accumulations reaching many tons annually.[30,31] PPW was collected, washed and dried at room temperature. The peels were washed and homogenized in distilled water, and the resulting slurry was filtered to remove the fibrous material. The filtrate was allowed to stand under ambient conditions to facilitate starch granule sedimentation. The slurry obtained from 1 L of distilled water at 30 °C was filtered through muslin cloth. The residue retained on the muslin was thoroughly rinsed with distilled water until the filtrate exhibited only minimal quantities of starch. Subsequently, the entire filtrate was collected in a glass beaker, and the residue on the muslin was discarded. The suspension in the beaker was allowed to settle undisturbed for 2 hours, during which a solid layer of starch sediment formed at the bottom.[32] This starch sediment was subjected to 3–4 washes with distilled water and then passed through a 120-mesh sieve until the rinsing water appeared clear, devoid of any suspended impurities. The resulting pure starch was then dried overnight in an oven at 40 ± 5 °C, ground, and finally sieved through a 150-mesh screen. The sediment was decanted, washed, and air-dried. Starch presence was confirmed by addition of Lugol's iodine solution, which induced a characteristic blue-black coloration indicative of amylose–iodine complex formation. Starch is selected as a binder in HGM fabrication due to its rich chemical functionality, natural abundance, and compatibility with polymeric hydrogel networks. Structurally, starch is a polysaccharide composed of amylose and amylopectin units, each bearing a high density of hydroxyl (–OH) groups. These –OH groups facilitate extensive hydrogen bonding with functional groups such as carboxylic acids (–COOH) and ethers (–O–) present in hydrogel matrices like hydroxypropyl cellulose (HPC) and poly(acrylic acid) (PAA). Beyond non-covalent interactions, under appropriate thermal or catalytic conditions, the hydroxyl groups in starch can also undergo esterification with carboxylic acid moieties in PAA, resulting in the formation of covalent cross-links that significantly enhance the mechanical stability and durability of the hydrogel network.

2.3 Synthesis of hydrogel

The HPC–PAA hydrogel was synthesized in accordance with the protocol delineated in our previous publication.[33] The hydrogel employed for membrane fabrication was prepared at the optimized pH of 5.5, as established in our prior investigations. Specifically, the pH was fine-tuned to reduce the LCST to ≤32 °C. This pH-optimized hydrogel formulation was subsequently utilized for the HGM fabrication.

2.4 Development of hydrogel membrane

Different weight percentages (%) of PPW extracted starch were weighed into a beaker, followed by adding 50 mL of distilled water, 15 mL of HCl (0.1 mol), and 2.5 mL of glycerol. The mixture was then heated on a hot plate and allowed to boil for 15 minutes under constant stirring. Subsequently, NaOH (0.1 mol) was incrementally added for neutralization, with each addition being assessed using indicator paper. The samples were further heated for an additional minute with continuous stirring with 10 mL of previously synthesized and optimized HPC–PAA hydrogel (pH 5.5).[33] The gelatinized suspensions were rapidly cast onto a flat Teflon mold using the emulsion templating technique. The starch suspensions were then dried at 60 °C in an oven for 24 hours. Films were subsequently incubated for 72 hours at 36 °C and a relative humidity of 60%. This process was repeated for all prepared samples. A comprehensive schematic depiction of the hydrogel membrane development from PPW is illustrated in Scheme 1. Upon subjecting a hydrogel comprised of dispersed starch powder to elevated temperatures, the starch undergoes gelatinization, forming interconnections between starch molecules. This process (gelatinization–retrogradation phenomenon) of starch

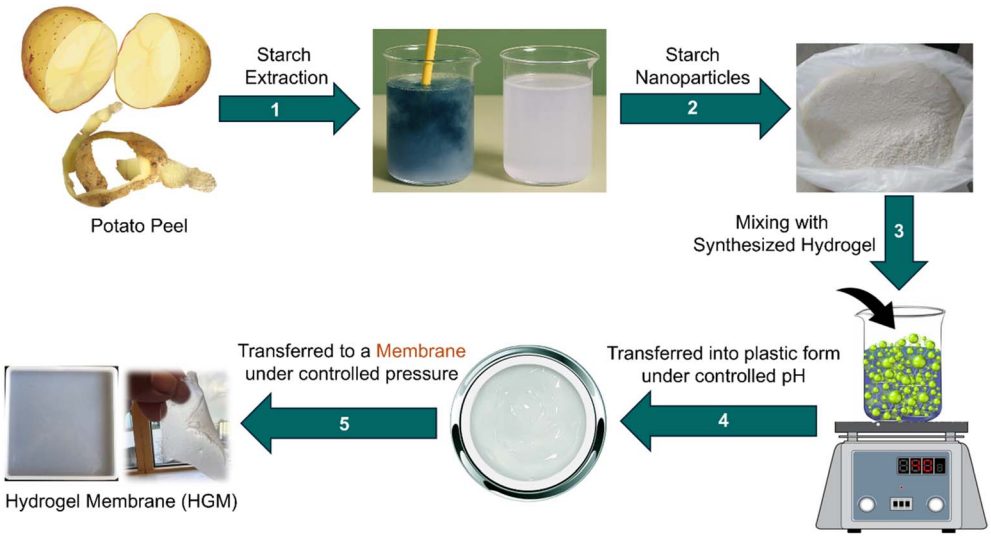

Scheme 1 Schematic representation of the hydrogel membrane development utilizing potato peel waste derived starch.

consolidation has been described, wherein starch powder is heated alongside a matrix material within an aqueous slurry, leading to the formation of a network of interconnected pores.

2.5 Materials characterization

The transmittance spectra of the HGM prototypes were recorded using a LAMBDA 1050 UV/vis/NIR spectrophotometer from PerkinElmer, spanning from 200 to 2000 nm. Temperature-dependent spectrophotometry measurements were conducted using a thermocouple to regulate heat for lower and higher temperatures, focusing solely on HGM samples. Microstructural analysis of hydrogel samples treated at various temperatures was performed using a scanning electron microscope (SEM), specifically an FEI Quanta FEG 650 under 5 kV. FTIR characterization was carried out using a LUMOS II ATR-FTIR microscope, Bruker and software OPUS version 8.8.4. The dynamic light scattering (DLS) measurements were performed using a Horiba NanoPartica-SZ 100 series. Porosity measurements were conducted using a mercury porosimetry analyzer from Quantacore Instruments, USA (model PM 60-GT-16).[34] The tensile test was conducted using a universal tensile testing machine (ZHIQU, Shanghai, China) under controlled conditions (temperature: 22.5 °C, humidity: 40%). The XPS data were acquired using a Kratos Axis SUPRA using monochromated Al K_α (1486.69 eV) X-rays at 15 mA emission and 12 kV HT (180 W) and a spot size/analysis area of 700 × 300 μm. The instrument was calibrated to gold metal Au 4f (83.95 eV) and dispersion adjusted to give a BE of 932.6 eV for the Cu $2p_{3/2}$ line of metallic copper. The Ag $3d_{5/2}$-line FWHM at a 10 eV pass energy was 0.544 eV. Source resolution for monochromatic Al K_α X-rays is ~0.3 eV. The instrumental resolution was determined to be 0.29 eV at 10 eV pass energy using the Fermi edge of the valence band for metallic silver. Resolution with a charge compensation system was <1.33 eV FWHM on PTFE. High resolution spectra were obtained using a pass energy of 20 eV, step size of 0.1 eV and sweep time of 60 s, resulting in a line width of 0.696 eV for Au $4f_{7/2}$. Survey spectra were obtained using a pass energy of 160 eV. Charge neutralisation was achieved using an electron flood gun with filament current = 0.4 A, charge balance = 2 V, and filament bias = 4.2 V. Successful neutralisation was adjudged by analysing the C 1s region wherein a sharp peak with no lower BE structure was obtained. Spectra have been charge corrected to the main line of the carbon 1s spectrum (adventitious carbon) set to 284.8 eV. All data were recorded at a base pressure of below 9×10^{-9} Torr and a temperature of 123 K. All data processing and peak fitting were carried out using CasaXPS software (version 2.3.20PR1.0). The test was performed with a tensiometer on the HGM samples, which had dimensions of 2 mm width, 6 mm length, and 1 mm thickness. Liquid hydrogel contact angle measurements were conducted by measuring the successive water contact angle (WCA) using a drop shape analyzer (Kruss DSA25) and the sessile drop method based on Young's equation. Each drop had a fixed volume of 5 μL, with a dosing rate of 500 μL min^{-1}. The instrument was equipped with a camera for image capture. The thermal conductivity measurements were performed using a C-Therm Trident system with a modified transient plane source. The method applied was the Modified Transient Plane Source technique following ASTM D7984-16.[35] To simulate conditions akin to 1 sun exposure, with an approximate light intensity of 1000 W m^{-2}, a Newport 66902 300 W xenon lamp, set at air mass (AM) 1.5, was employed.[36] Heat flux flow through the window glazing samples and indoor and outdoor temperatures were monitored and recorded using a FluxTeq COMPAQ data acquisition system, having voltage resolution < 1 μV. For *U* value measurements of windows, a FluxTeq PHFS-OEM heat flux sensor (nominal sensitivity: 2.5 mV W^{-1} cm^{-2}) and FluxTeq's thin-film foil surface T-type thermocouple (specific thermal resistivity: ≈0.84 K kW^{-1} m^{-2}) were utilized.[37] The Raman spectra of HGM were obtained using a WITec Alpha 300R Raman microscopy system.

3. Experimental results

3.1 Research design

Fig. 1 presents a schematic representation of the HGM integration strategy and its subsequent performance assessment in the built environment. The synthesized HGM is embedded within the interspace of a double-glazed window unit, effectively addressing typical limitations associated with hydrogel-based systems, such as fluid leakage and long-term evaporation. This membrane-based configuration facilitates seamless retrofitting without necessitating structural modifications. Thermal transmittance and temperature distribution profiles were evaluated using a custom-designed hot-box chamber, in comparison with both conventional glazing systems and alternative HGM configurations. A photographic series of HGM samples containing various wt% starch illustrates the tunability of optical transparency and mechanical robustness, highlighting the role of starch as a sustainable reinforcing agent. Additionally, a commercial silicon PV module was directly interfaced with the HGM-integrated glazing as an integrated glazing unit (IGU) and subjected to performance testing under varying solar irradiation conditions.

3.2 Temperature dependent transparency analysis and durability test

To investigate the optical properties of HGMs, varying concentrations of starch, such as 1, 3, 5, and 10%, were incorporated into a hydrogel matrix, and their transmission characteristics were systematically examined. Fig. 2a presents the UV-vis-NIR transmission spectra (200–2500 nm) of all samples. A pronounced decrease in transmittance within the NIR region was observed with increasing starch content. This trend indicates that higher starch loading leads to enhanced light scattering or absorption, thereby diminishing NIR transmittance. In contrast, transmittance in the visible range remained relatively high (>75%) for samples containing lower starch concentrations (1 and 3%). However, as the starch content increased to 5%, visible transmittance dropped to approximately 50%, and a further increase to 10 wt% resulted in a dramatic reduction to around 20%. This decline in optical transparency is primarily attributed to haze formation within the hydrogel matrix.

Starch, a naturally occurring polysaccharide primarily composed of amylose and amylopectin, inherently promotes haze due to its complex structural and physicochemical characteristics. Its semi-crystalline nature, comprising both amorphous and crystalline domains, leads to light scattering because of refractive index mismatches. Additionally, starch's high hydrophilicity facilitates significant water absorption, inducing swelling and potential microphase separation. These effects generate additional scattering centres, further reducing optical clarity. Moreover, incomplete gelatinization or aggregation of starch granules can result in undissolved or partially solubilized particles that act as scattering inhomogeneities. In composite systems, incompatibility between starch and the surrounding hydrogel matrix can lead to microdomain formation, exacerbating phase separation and disrupting uniform light transmission. Consequently, the overall optical behaviour is dictated by the extent of these structural heterogeneities. The order of maximum visible light transmission is: 10% ≪ 5% ≪ 3% < 1%, while the inverse trend is observed for minimum NIR transmission, indicating enhanced scattering or absorption in samples with higher starch content.

Considering the trade-off between maintaining high visible light transmittance and minimizing NIR transmission, the hydrogel–starch composite containing 3% starch was selected for further investigation. This composition exhibited an optimal balance between optical clarity and infrared-blocking performance. Accordingly, Fig. 2b displays digital photographs of the 3% HGM, illustrating its thermoresponsive

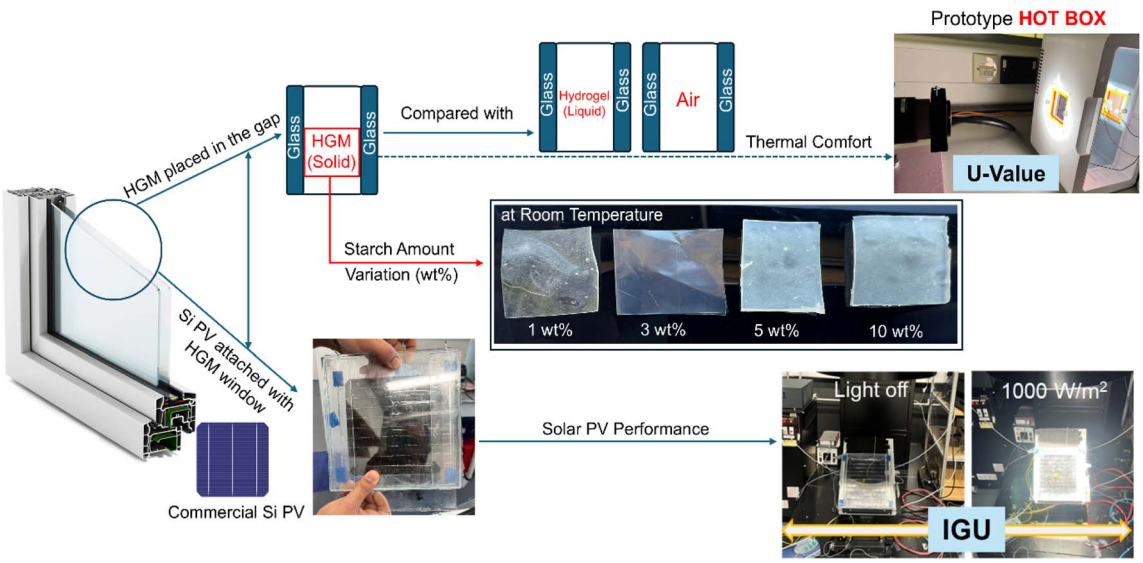

Fig. 1 Schematic overview of HGM integration and performance evaluation, illustrating the research design of this study.

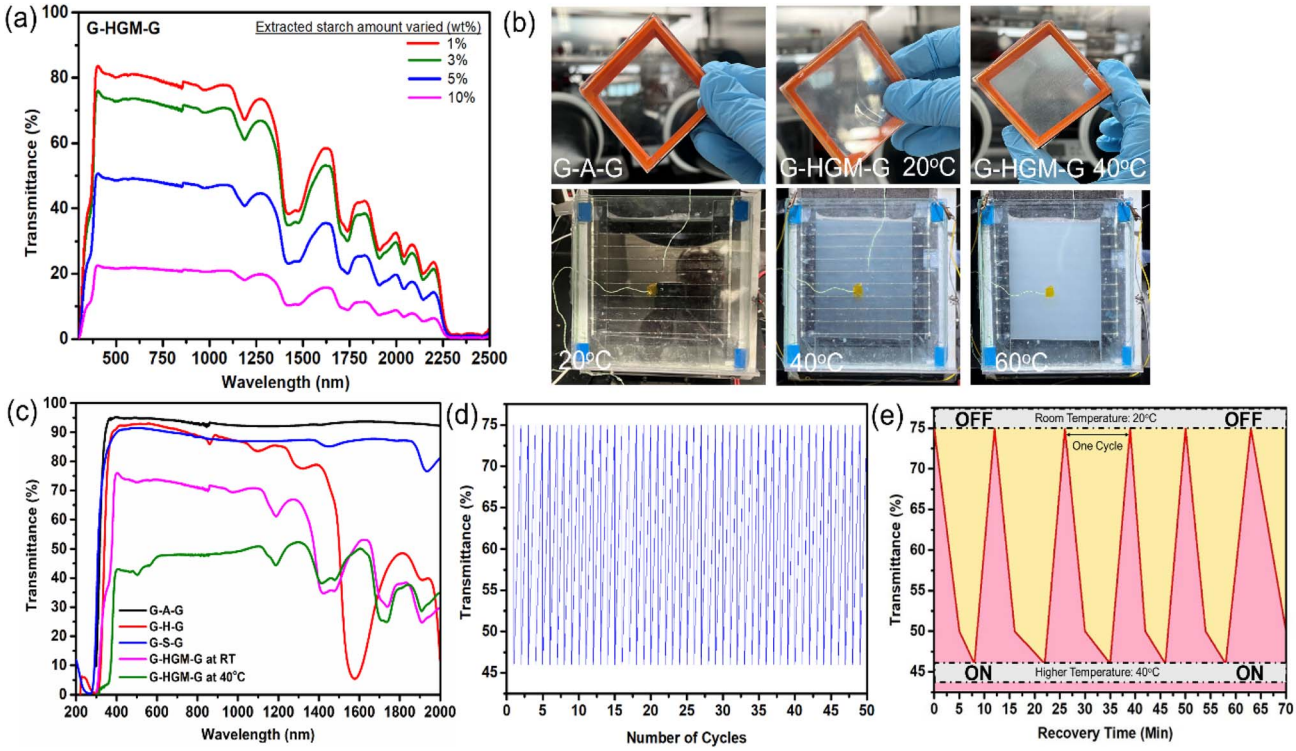

Fig. 2 (a) Optical transmittance spectra of HGM composites incorporating varying concentrations of extracted starch, (b) representative digital photographs of the optimized 3% HGM sample integrated into both a prototype window and a PV module, illustrating its thermotropic response at ambient and elevated temperatures, (c) comparative transmittance spectra of the optimized 3% HGM configuration against alternative window composites, highlighting spectral modulation under different compositional conditions, (d) thermal cycling performance of the optimized HGM sample, demonstrating the stability and reversibility of optical properties over repeated heating–cooling cycles, and (e) dynamic optical switching behaviour of the optimized HGM system, indicating reversible transmittance modulation and quantifying the associated recovery time.

optical behaviour. The abbreviations are defined as follows, representing the prototype double-glazed model window configurations:

- G–A–G: glass–air–glass.
- G–H–G: glass–hydrogel–glass.
- G–S–G: glass–starch (melted)–glass.
- G–HGM–G: glass–hydrogel membrane–glass.

The membranes demonstrated a distinct transition from a transparent to a translucent state as the temperature increased, indicating thermally induced structural rearrangements within the hydrogel matrix. A similar transparency modulation was observed when the same 3% HGM membrane was integrated with a silicon PV device and subjected to prolonged solar simulation. The corresponding images confirm that the optical transition persists under real-world solar exposure conditions, suggesting potential utility in smart window or light-regulating photovoltaic applications.

Fig. 2c presents a comparative analysis of various window configurations fabricated using the optimized 3% composite formulation. The G–A–G configuration demonstrates superior optical performance, achieving transmittance levels as high as 95% across the visible to near-infrared (vis-NIR) spectrum. In contrast, substitution with gelatine extracted starch derived from PPW results in a marginal decline in visible-NIR transmittance to approximately 85–90%. Among the evaluated configurations, G–A–G consistently exhibits the highest transmittance across the entire spectral range, maintaining values above 90%, which reflects exceptional optical clarity and minimal intrinsic absorption. Configurations incorporating G–H–G and G–S–G exhibit moderately reduced transmittance (~85–90%) relative to G–A–G. Notably, the G–H–G variant displays distinct absorption features in the 1400–2000 nm range, likely attributable to overtone and combination bands associated with O–H and C–O–H vibrational modes or residual water content intrinsic to the hydrogel matrix. In sharp contrast, the thermoresponsive G–HGM–G configurations, analyzed both at room temperature (RT) at 20 °C and at 40 °C—exhibit markedly attenuated transmittance in the NIR region, suggesting their applicability for solar modulation functionalities. At RT, G–HGM–G maintains visible transmittance near 70%, but shows significant absorption beyond 1200 nm. Upon thermal activation at 40 °C, a substantial decline in transmittance is observed, particularly within the NIR domain, where values decrease to approximately 40% or lower. This pronounced shift implies a temperature-triggered optical modulation, potentially arising from phase transitions or conformational rearrangements within the hybrid microgel network. Typical UV absorbance is observed below 220 nm, mainly due to $\pi \rightarrow \pi^*$ or $n \rightarrow \pi^*$ transitions in any minor organic residues.[38] Collectively, these findings highlight the

tunable and thermoresponsive optical characteristics of G–HGM–G systems, underscoring their suitability for deployment in smart window applications requiring dynamic, temperature-regulated light transmission.

Further, Fig. 2d illustrates the thermal cycling performance of the G–HGM (3%) composite film, evaluated up to 50 successive heating–cooling cycles. Transmittance was measured at a fixed wavelength at 550 nm to monitor the reversible optical switching behaviour of the sample under repeated thermal stimuli. The initial transmittance at ~20 °C is approximately 75%, corresponding to a highly transparent state. Upon heating to 40 °C, the transmittance consistently decreases to around 46%, indicating a significant reduction in optical transparency and a transition to a translucent state. This reversible change in transmittance confirms the thermoresponsive nature of the composite, likely due to the phase transition or structural rearrangement of the functional polymer–HGM matrix. Notably, the transmittance modulation remains stable and reproducible over 50 consecutive thermal cycles, with no observable degradation or hysteresis in performance. This strong cycling stability highlights the excellent durability and robustness of the 3% HGM composites, making it a promising candidate for long-term applications in smart window systems or thermal-switching coatings where sustained performance under fluctuating environmental conditions is essential.[39]

Consequently, the dynamic switching characteristics of the same sample over multiple on–off thermal cycles, with real-time monitoring of optical transmittance at a fixed wavelength of 510 nm (considered as CIE photopic luminous human eye efficiency, photopic vision), is shown in Fig. 2e. The transmittance data were recorded continuously for a total duration of 70 minutes to assess the switching speed and reliability of the thermal response. Each cycle consists of heating the film at 40 °C (transitioning to the translucent state) and then cooling it back to room temperature (20 °C) to recover transparency. At room temperature, the film exhibits a high transmittance of ~75%, while heating reduces the transmittance to ~45%, consistent with the optical modulation observed in earlier thermal cycling tests. The plot shows that each full switching cycle from transparent to translucent and back is completed in approximately 12 minutes. The consistent amplitude and repeatability of the transmittance change over all cycles indicate excellent thermal reversibility, quick response time, and structural stability under repeated thermal stimulus. This result further confirms the durability and responsiveness of the composite, making it highly suitable for practical smart window applications where rapid and repeated modulation of light transmittance in response to ambient temperature changes is required.

3.3 Microstructural analysis

Following SEM microstructural analysis, quantitative evaluation of pore size distribution is critical for elucidating the stimuli-responsive mechanisms underlying the thermotropic behaviour. Fig. 3a and b depict the HPC–PAA hydrogel, characterized by a cloudy morphology comprised of fine polymer nanoclusters. In contrast, incorporation of starch into the hydrogel matrix to form composite membranes induces substantial microstructural transformations. Specifically, Fig. 3c and d show the 1% and 2% HGM samples, respectively, which exhibit a stiff, fibrous network embedded with starch. This fibrous network becomes increasingly perforated and exhibits a roughened texture with increasing starch content, indicative of poor interfacial compatibility and the formation of porous domains within the composite architecture with the micron-sized wrinkles. At 3% starch loading (Fig. 3e and f), the microstructure reveals a pronounced fibrous network, particularly evident at the membrane edge (Fig. 3e, magnified view at the edge), confirming successful starch embedding within the hydrogel matrix. However, further increases in starch concentration to 5% and 10% lead to pore filling by excessive starch, resulting in a dense, trench-like composite morphology devoid of distinct porous features or well-defined fibrous structures. Starch can interact with the hydrogel polymers (through intermolecular H-bonding or other interactions like bifurcated or multicentered H-bonding), making the polymer network more

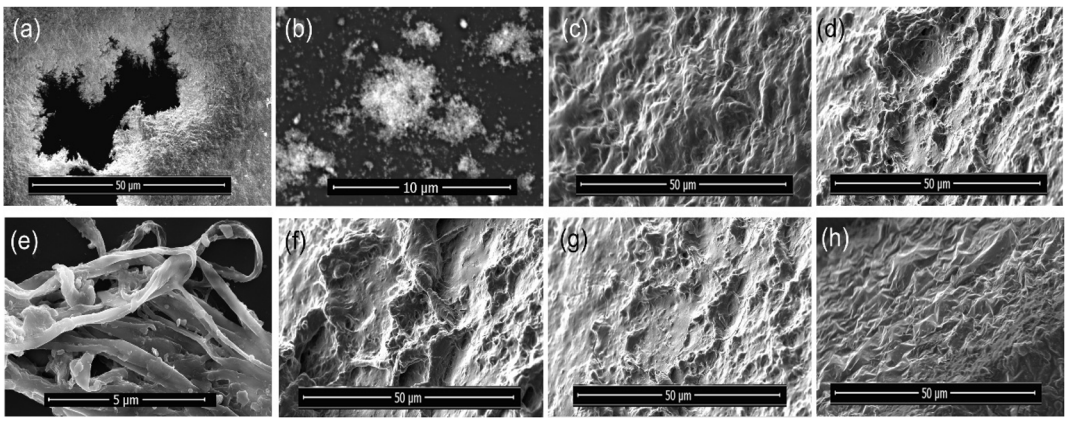

Fig. 3 SEM micrographs illustrating the microstructural evolution of HGM composites with varying starch content: (a and b) HPC–PAA hydrogel at different magnifications; (c) 1% and (d) 2% starch-added HGM samples, (e and f) 3% starch-added HGM samples at different magnifications; (g) 5% and (h) 10% starch-added HGM samples, highlighting changes in network morphology and porosity with increasing starch concentration.

compact and less open. This tighter structure leads to fewer and smaller pores. This morphological evolution effectively smooths previously sharp and porous characteristics, likely influencing the optical and mechanical properties of the composite.[40,41] Thus, based on the correlation between porosity, network architecture, and reinforcement characteristics, the 3% HGM sample exhibited an optimal balance of structural integrity and optical properties, demonstrating a pronounced misting effect, and was consequently selected for further investigation.[42]

3.4 Wettability, porosity and mechanical stability analyses

Fig. 4a illustrates the static water contact angle measurements of HGM incorporating varying concentrations of starch, revealing a clear trend of decreasing surface wettability with increasing HGM content. At 1% HGM, the membrane exhibits a low contact angle of 17.7°, indicative of a highly hydrophilic surface. However, as the HGM concentration increases to 3% and 5%, the contact angles rise markedly to 46.2° and 67.6°, respectively, signifying a progressive transition toward hydrophobicity. This shift in wettability is primarily attributed to the intrinsic surface properties of the HGM, which possesses rough shells that are relatively hydrophobic compared to the less starch-based hydrogel matrix an observed from the SEM microstructure analyses from Fig. 3. The increased incorporation of HGM likely reduces the availability of hydrophilic hydroxyl groups on the membrane surface by either masking or displacing them, thus diminishing the membrane's affinity for water. The inclusion of HGM can alter surface roughness, potentially creating micro-scale heterogeneities that trap air beneath droplets (Cassie–Baxter state).[43,44] Collectively, these findings suggest that the integration of HGM alters both the chemical composition and the physical structure of the membrane surface, leading to a significant reduction in hydrophilicity as the HGM content increases. Alternatively, Fig. 4b represents the variation in WCA of hydrogel membranes containing 3% and 5% HGM over a 30-day immersion period, and it directly complements the static contact angle measurements as shown in Fig. 4a. Over time, however, the WCA of the HGM 3% membrane decreases significantly, stabilizing at around 25° by the end of the 30-day period. In contrast, the HGM 5% membrane maintains a relatively stable WCA throughout the immersion period, showing only a slight decline from ~68° to ~66°. This trend indicates that the HGM 3% membrane undergoes substantial surface rehydration or structural rearrangement during prolonged exposure to water, resulting in increased surface hydrophilicity. This may be due to gradual leaching or redistribution of loosely bound HGMs, swelling of the hydrogel matrix, or reorientation of polar functional groups (*e.g.*, hydroxyl groups from starch) toward the surface. Conversely, the HGM 5% membrane exhibits high resistance to such changes, likely due to a denser surface coverage or encapsulation effect by the HGMs, which inhibits water penetration and restricts exposure of hydrophilic moieties.[45,46] Overall, the figure underscores the influence of HGM content not only on the initial wettability but also on the long-term stability of the surface characteristics in aqueous environments. Lower HGM content allows for dynamic restructuring and increased hydrophilicity upon immersion, whereas higher HGM loading results in a more hydrophobic and temporally stable surface.

Introducing porosity into a material represents a straightforward and efficacious strategy for attaining low thermal conductivity. This arises from the capability of pores to impede thermal transport within solids through the reduction of cross-sectional area and the augmentation of heat transfer pathway tortuosity. Notably, an irregular distribution of membrane

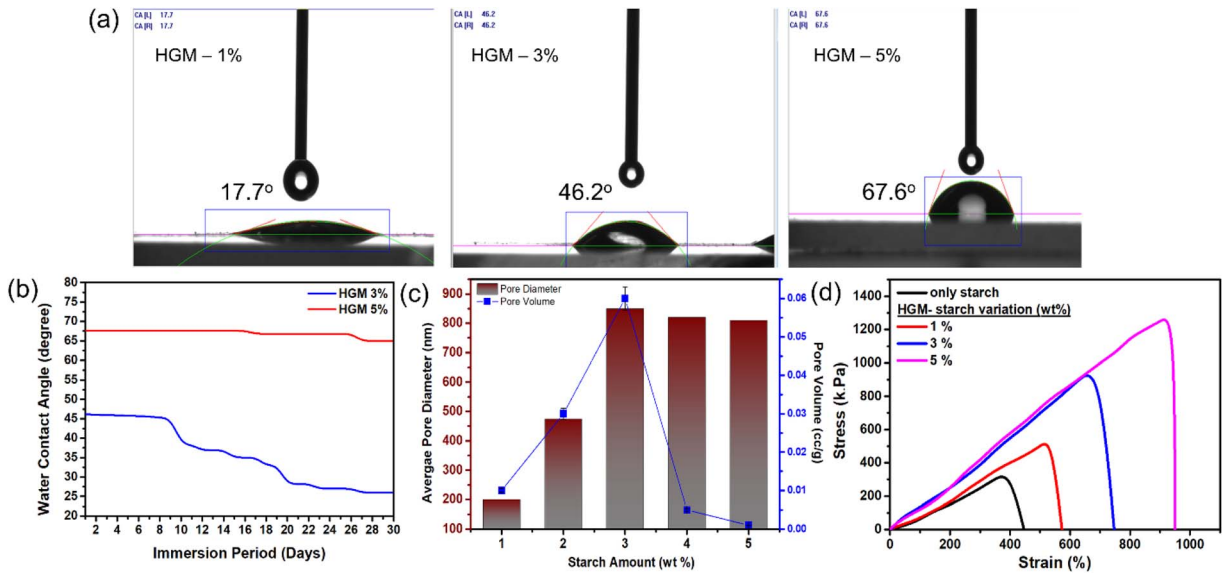

Fig. 4 (a) Digital images of water contact angles for HGM-based samples with varying starch content, (b) wettability stability plots comparing the temporal behavior of 3% and 5% HGM samples, (c) a comparative plot for the pore size and pore volume and (d) tensile stress–strain curves of HGM composite samples, respectively.

pores is anticipated to manifest as wedge-like arrangements. As the starch content increases, both the average pore diameter and pore volume initially rise, reaching a maximum at 3%, where the material exhibits the highest pore volume (~0.06 cc g^{-1}) and largest pore size (~850 nm) as shown in Fig. 4c. This optimal structure enhances thermal insulation by increasing the air content within the matrix, effectively reducing thermal conductivity due to air's low thermal conductivity. Beyond 3%, further starch addition leads to a steady decline in pore volume, despite relatively stable pore diameters, indicating possible pore collapse or densification that hinders the formation of an interconnected porous network.[47,48] This reduction in effective porosity increases heat conduction pathways through the solid matrix, diminishing the thermal insulation benefits. In contrast, at higher starch concentrations (5–10%), although the pore diameter remains relatively large, the pore volume drops sharply, suggesting a denser and more compact structure with limited water permeability. This structural densification corresponds to the stable and higher contact angles observed for the HGM 5% membrane, reflecting persistent surface hydrophobicity and minimal interaction with water. Notably, while the localized pore volume and diameter may increase due to starch-induced structural rearrangement, the overall matrix porosity decreases as starch progressively fills and densifies the hydrogel network. Therefore, the 3% starch sample represents the optimal formulation, achieving a well-balanced porous architecture that minimizes heat conduction and maximizes insulation efficiency. Further, the HGM exhibited remarkable mechanical flexibility, capable of withstanding a variety of deformations including stretching, knotting, twisting, and compression. As illustrated in Fig. 4d, the mechanical properties of the HGM were significantly influenced by the starch content. Both the maximum strain (S_m) and the breaking stress (S_f) of the HGM increased with the starch concentration. Specifically, when the starch content reached 1%, the maximum strain and breaking stress attained values of 575% and 520 kPa, respectively. This represents a 40% increase in maximum strain and a 125 kPa increase in breaking stress compared to those of only starch. The incorporation of starch into the polymeric network of the hydrogel facilitated the formation of a more intricate crosslinked structure, thereby enhancing both S_m and S_f. At ambient temperature, the hydrodynamic diameter of the hydrogel was measured to be approximately 1 μm. However, with increasing temperature, this size expanded significantly to around 1.5 μm. Notably, the hydrodynamic size exhibited considerable variability depending on the operating temperature, undergoing substantial changes at both lower and higher temperatures compared to room temperature. This observation indicates a dynamic, temperature-dependent response in the hydrogel's structural behaviour. The phenomenon suggests a complex interplay between temperature and the aggregation mechanisms of the hydrogel constituents.[49] Specifically, at elevated temperatures, the aggregation process appears to be predominantly influenced by PAA, resulting in larger hydrodynamic dimensions. In contrast, at lower temperatures, the aggregation dynamics seem to be driven by HPC, potentially due to changes in osmotic pressure, which modulate the hydrogel's hydrodynamic size. These findings underscore a temperature-dependent shift in the dominance of aggregation mechanisms within the hydrogel matrix, providing critical insights into its adaptive behaviour and functional properties.[50] At a starch concentration of 5 wt%, S_m further increased to 946%, while the corresponding maximum S_f reached 1264 kPa. This enhancement is attributed to a substantial increase in the crosslink density within the network, which contributed to the observed rise in stiffness and elasticity. However, the increase in starch content, while beneficial for mechanical strength, led to a reduction in transparency (Fig. 2a), a crucial parameter for the intended applications of HGM. A passive smart window with an adjustable phase transition temperature was demonstrated, exhibiting good flexibility and stability.

3.5 Thermal conductivity analysis

Thermal conductivity measurements for 3% HGM were conducted to elucidate their heat-insulation efficacy, juxtaposed with starch and conventional glass, as depicted in Fig. 5a. HGM demonstrated significantly lower thermal conductivity at 0.23 W m^{-1} K^{-1}, contrasting with starch at 0.81 W m^{-1} K^{-1} and glass at 1.05 W m^{-1} K^{-1}. Notably, negligible alterations in thermal conductivity were observed with increasing temperatures up to 60 °C, aligning with maximum outdoor temperature scenarios, indicative of sustained insulation properties across elevated temperatures. Gradient crosslinking sites may arise from the crosslinking reaction within the HGM, leading to the random formation of a contiguous pore gradient spanning from macropores to nanopores throughout the polymeric network. When immersed in water, the circular gradient hydrogel sheet exhibits rapid and reversible shape transformations in response to temperature variations between 60 °C and 20 °C. This phenomenon engenders the tortuosity effect, enabling control over transparency and thermal behaviour.[51] Tortuosity serves as a metric to characterize the structural intricacies and approximate the length of pathways and time required for the dispersion of heat flow. Various forms of tortuosity, such as geometric, hydraulic, electrical, and diffusive, have been elucidated in the existing literature. In the context of the sponge-like polymer, tortuosity delineates the trajectory of heat flux traversing the broader inter-pore spaces. Consequently, this parameter reflects the relationship between the diffusion coefficient of heat flux in the absence of porous confinement and its effective diffusion coefficient under porous confinement. At a temperature of 20 °C, the 3% HGM sample, characterized by its stable and transparent polymeric network, exhibits minimal tortuosity. However, as the shape and structure of the matrix undergo gradual changes, this low tortuosity can gradually impede heat flow.

Additionally, temperature elevation may lead to decreased pore size and alterations in the percolation of the gel network. These changes can create a barrier that restricts heat flow and induces higher tortuosity. As porosity increases, the fraction of air-filled voids increases, reducing overall thermal conductivity since air has a much lower thermal conductivity than most polymers. However, a high porosity alone does not guarantee

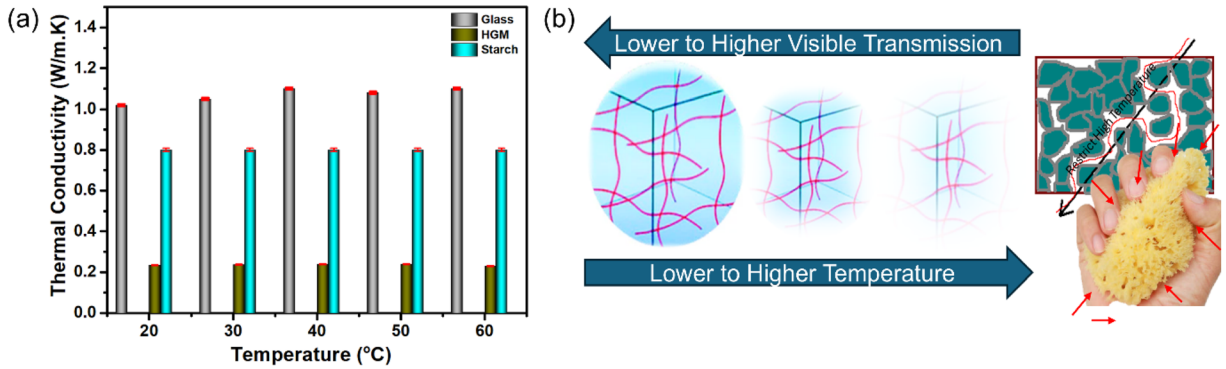

Fig. 5 (a) Temperature-dependent thermal conductivity measurements of HGM compared with starch and ordinary glass, and (b) a plausible mechanism explaining the heat shielding and maintenance of indoor thermal comfort by HGM for various temperatures in the window application.

low conductivity if tortuosity is low (direct paths). Fig. 5b illustrates a schematic representation of the probable heat-shielding mechanism of the HGM across various temperatures while tuning its visible transparency. The investigation into spherical pore sizes revealed that the thermal conductivity of porous materials is lower when the pore shape is closer to spherical compared to when it deviates from a spherical shape. Additionally, assuming isotropic polymeric spherical pores tends to underestimate the thermal conductivity of porous composites. In contrast, the relationship between pore shape and percolation threshold, as well as tortuosity, exhibits an inverse pattern to its impact on effective thermal conductivity.[52,53] Both the thermal conductivity and tortuosity of the material varied with porosity following a power-law relationship.

3.6 Cryo-XPS and ATR-FTIR microscopic analysis

The high-resolution cryo-XPS core-level spectrum of the C 1s and O 1s regions provides unequivocal evidence for the formation of covalent chemical crosslinks between the hydrogel matrix and incorporated starch. In the pristine HPC–PAA hydrogel (Fig. 6a and d), the C 1s spectrum shows three main components: C1 (~284.8 eV) corresponding to C–C/C–H bonds from the cellulose and acrylic backbone, C2 (~286.5 eV) from C–O groups typical of hydroxyls and ethers in HPC, and C3 (~288.9 eV) representing carboxyl (O–C=O) functionalities in PAA. Similarly, the O 1s spectrum displays O1 (~531.8 eV) from carbonyl oxygens, O2 (~533.1 eV) from hydroxyl and ether oxygens, and O3 (~534.6 eV) associated with adsorbed water or weakly bound –OH groups. Upon addition of 3% starch (Fig. 6b and e), an increase in the intensity of C2 and O2 components is

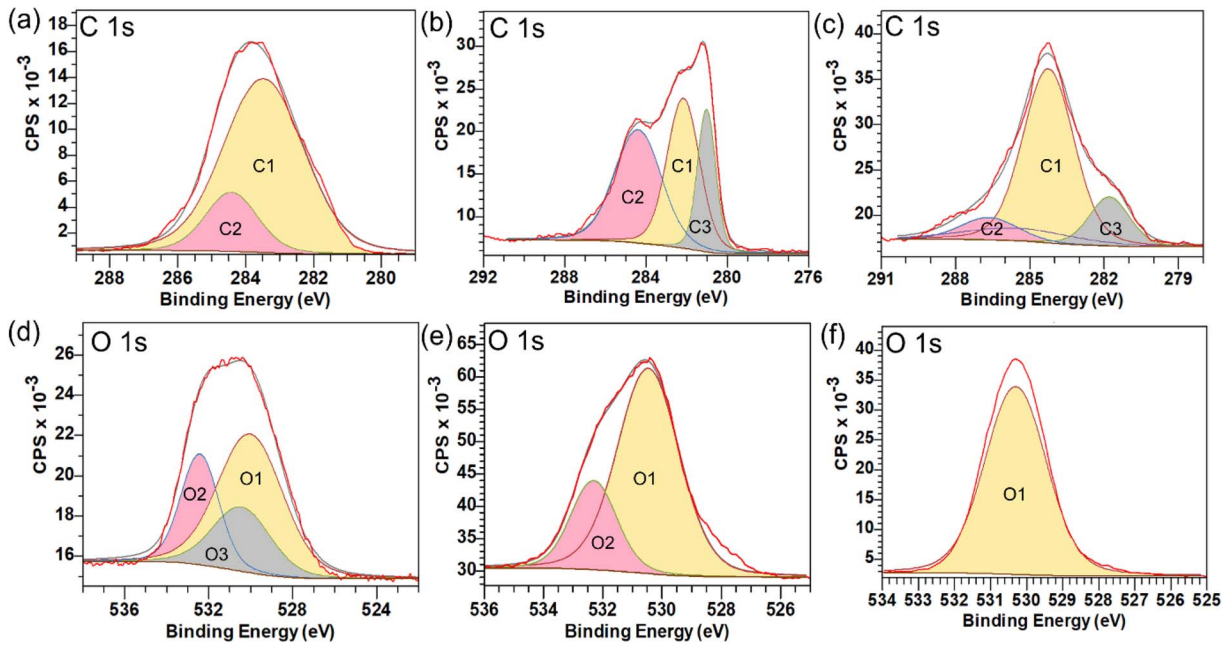

Fig. 6 XPS core-level spectrum of C 1s and O 1s for (a and d) the pristine hydrogel, and (b and e) 3% and (c and f) 5% HGM samples, respectively.

observed due to the introduction of starch's abundant hydroxyl groups. Simultaneously, the C3 and O1 peaks shift to slightly lower binding energies (~0.3–0.4 eV), indicating the formation of hydrogen bonds between starch –OH groups and PAA carboxylic acids. A new low-binding-energy shoulder in the C 1s spectrum (~280.5 eV) also appears, suggesting possible esterification occurring during thermal curing. With 5% starch (Fig. 6c and f), these effects are further amplified: the C2 component becomes more dominant, reflecting the polysaccharide-rich environment, and both C3 and O1 peaks continue to shift and broaden, consistent with enhanced hydrogen bonding and increased cross-linking density. The disappearance of the O3 peak implies reduced free water content due to network densification. These core-level spectral changes confirm that starch incorporation into the HPC–PAA hydrogel leads to the formation of a robust dual cross-linked network, stabilized through extensive hydrogen bonding and a minor but significant contribution from covalent ester linkages resulting in the formation of a structurally reinforced membrane.[54,55]

The ATR-FTIR (Fig. 7a) spectra reveal significant structural changes in HGM compared to native starch, confirming the formation of a stable, chemically crosslinked matrix. Native starch has a granular structure with microvoids and free hydroxyl groups. Upon adding HPC and PAA, these polymers infiltrate and fill the microstructural gaps, leading to a denser, more continuous hydrogel network. The broad peak around 3340 cm^{-1}, corresponding to O–H stretching vibrations, becomes more intense and broader in HGM samples significantly for 3% HGM and further samples, indicating enhanced H-bonding and moisture retention. These changes reflect the establishment of new H-bonds and possibly ester or ether linkages due to interaction between the hydroxyl groups of starch and carboxyl groups of PAA. This indicates that the added polymers are not just physically embedded but are chemically interacting, consistent with the filling effect.[56,57] As crosslinking progresses, these hydroxyl groups become involved in intermolecular interactions or are sterically hindered, resulting in a quenching of the broad O–H band typically observed in unmodified starch. The decrease in intensity of the O–H band also supports the idea that hydroxyl groups are being consumed in the formation of new bonds, suggesting effective filling and bonding between phases.[58] Peaks at 2935 and 2865 cm^{-1} represent C–H stretching from alkyl chains, with increased intensity in HGM samples, confirming polymeric additive incorporation. The new peak at 1716 cm^{-1} in HGM spectra, absent in native starch, corresponds to C=O stretching from carboxylic groups in polyacrylic acid, confirming further chemical crosslinking. The peak at 1445 cm^{-1} (CH_2 bending) further supports this. Shifts and variations in intensity within the fingerprint region, specifically at 1096, 1025, and 918 cm^{-1}, are associated with C–O–C and C–O–H stretching vibrations characteristic of starch and cellulose. These spectral changes indicate structural rearrangements and the possible formation of ether linkages. This observation is consistent with the hydrogen bonding absorption features identified through XPS analyses. An additional absorption peak was observed at 1648 cm^{-1}, which is characteristic of starch. This peak arises from the first overtone of O–H bending vibrations, coupled with the stretching vibrations of the C–O–C ether linkages. This suggests that the polymer concentration is ideal for filling the matrix without phase separation or saturation, yielding a highly crosslinked, mechanically coherent hydrogel network.[59] As the starch content increases, these structural units become more abundant, leading to intensified absorbance in these regions, particularly reflecting the contributions of starch and associated polymers in the hydrogel matrix. Therefore, the 3% HGM sample shows the most pronounced peaks across these regions, indicating optimal crosslinking density and a stable hydrogel matrix, outperforming higher or lower concentrations.

Fig. 7b presents the corresponding microscopic images acquired during the ATR-FTIR mapping analysis. The coloured dots in the images represent different regions within the hydrogel matrix from which spectra were recorded, and the

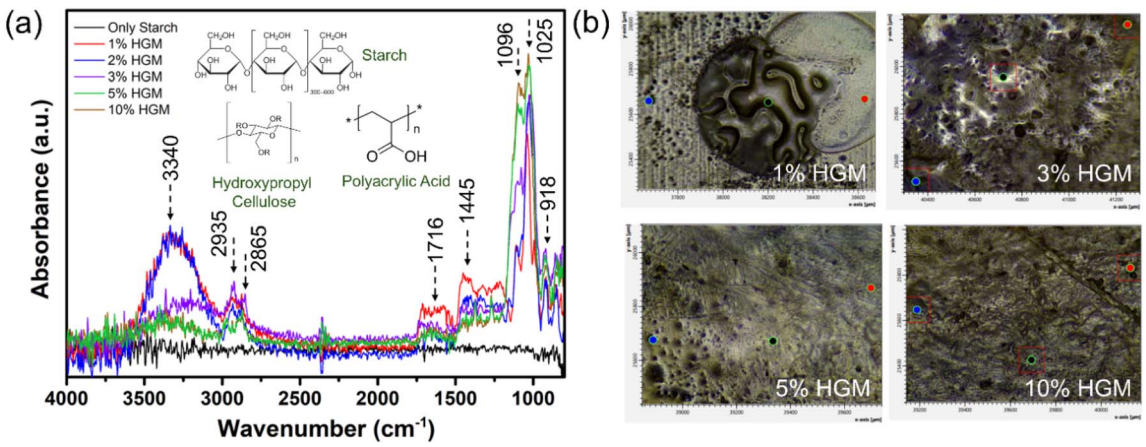

Fig. 7 (a) ATR-FTIR spectra of HGM samples with varying starch content compared to native starch (inset: the molecular structures of the primary components of HGM), (b) corresponding microscopic images acquired during ATR mapping, where coloured dots represent different regions sampled for spectral averaging.

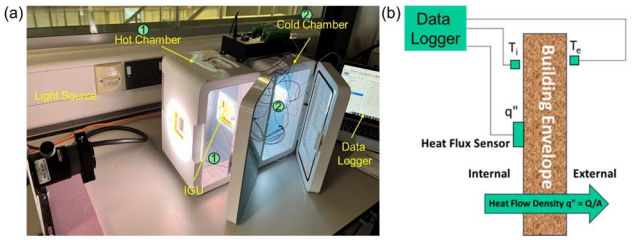

Fig. 8 (a) Photograph of the prototype hot–cold box setup to measure the *U*-value of the HGM as a window component and (b) corresponding schematic view of the measurement set-up inside the chamber.

overall signal reflects the averaged spectrum shown in Fig. 8a. Interestingly, the 3% HGM sample exhibits visibly higher porosity, indicating a more open and less compact structure. As the starch content increases beyond 3%, the hydrogel becomes progressively denser, and the visible porosity diminishes. This observation resonates with the spectral evidence of enhanced polymer filling and crosslinking at higher starch concentrations, where the network becomes more compact due to excessive filler content. The morphological changes seen in the ATR-mapping images are consistent with SEM analysis, further corroborating that 3% HGM strikes an optimal balance between crosslinking and porosity.

3.7 Calorimetric hot–cold box experimental setup and measurements

HGM was introduced into the space between two conventional low-iron glass panes to assess its thermal performance for indoor comfort analysis. Fig. 8a illustrates a photograph of a prototype setup utilized for testing the thermal transmittance (*U*-value) of the HGM window prototype. A "hot–cold box" represents a controlled experimental apparatus employed to assess the thermal characteristics of a window by determining its *U*-value. The *U*-value, also called thermal transmittance, quantifies the heat transfer rate through a building component under standardized conditions, indicating its insulating efficacy against heat flow, with lower *U*-values signifying superior insulation.[53]

Within our prototype hot–cold box setup, as depicted in Fig. 8a, the HGM component under evaluation is positioned between two regulated environmental chambers – one heated and one cooled, to establish a temperature gradient across the component. Subsequent heat flow measurement through the component is conducted using temperature and heat flux sensors. By precisely controlling the environmental parameters and accurately measuring the heat flux, researchers can ascertain the *U*-value of the HGM component for temperature profile measurements.

The *U*-value measurements were conducted in accordance with the ISO 9869:2014 average standard method and adapted for the prototype hot–cold box as shown in Fig. 8b.[37] To avoid negative *U*-values, consider the absolute value $|T_i - T_e|$ in the following equation (eqn (1)),

$$U = \frac{q''}{|T_i - T_e|} \quad (1)$$

where q'' = heat flux; T_i = interior temperature; T_e = exterior temperature; if $T_i > T_e \rightarrow q''$ is leaving the wall; if $T_i < T_e \rightarrow q''$ is entering the wall.

The effect of illumination equivalent to 1 sun on indoor temperature was investigated, comparing a window incorporating HGM with one filled solely with the hydrogel. The HGM window demonstrated a moderate reduction in temperature, averaging approximately 30 °C, measured at locations 1 and 2 as mentioned in Fig. 9. Conversely, the window filled only with hydrogel exhibited a successive temperature increase, reaching approximately 20 °C as consistently measured over a 60 minute exposure period. Additionally, Fig. 9 indicates the HGM window's ability to consistently maintain indoor thermal comfort levels throughout the day, contrasting with external temperature fluctuations.

The HGM windows demonstrate a *U*-value of 1.84 W m^{-2} K^{-1}, representing an approximate reduction of 33% compared to standard double-glazed windows filled with argon. Consequently, individual components comprising the HGM have undergone detailed examination to determine the *U*-value of the prototype window. Results indicate that all components exhibit *U*-values ranging from 20% to 70% higher than those of HGM windows. Table 1 presents the comprehensive *U*-value measurements alongside the relative indoor–outdoor temperature gradient, providing initial insights into the efficacy of reducing the *U*-value to maintain a higher temperature gradient between indoor and outdoor environments. The diminishment of accuracy in *U*-values for small samples, attributed to the edge effect, is noteworthy. This diminution is particularly evident in our samples, which measure only 6 cm × 6 cm. However, as sample size increases, the influence of the edge effect diminishes, resulting in more precise values. Our analysis of hot-box development measurements reveals a discernible trend in *U*-

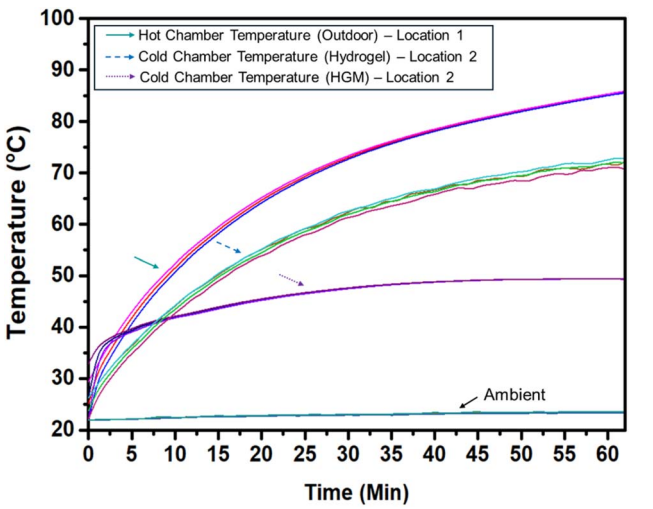

Fig. 9 Comparison of simultaneous temperature profiles between the IGU and the only hydrogel-filled window, as measured in a hot-box chamber.

Table 1 A comparative study to enhance *U*-value determination of a prototype window development using HGM compared with its relative components

Prototype window configuration (4 mm × 12 mm × 4 mm)	*U*-Value ($W\ m^{-2}\ K^{-1}$)	Interior–exterior temperature gradient (°C) ± 0.05
Glass–air–glass	3.12	0.02
Glass–argon–glass	2.45	22
Glass–water–glass	7.39	10
Glass–hydrogel–glass	2.32	20
Glass–HGM–glass	1.84	30

values, highlighting the significance of material composition and its impact on *U*-value measurements. This reduction of approximately 33% in the *U*-value signifies that the HGM windows are significantly more efficient at retaining heat indoors during colder months and preventing heat from entering during warmer months. This improvement in thermal performance translates to reduced energy consumption for heating and cooling purposes, thereby potentially leading to lower utility bills and decreased environmental impact.

3.8 Hydrogel membrane as an integrated glazing unit for silicon photovoltaic cells

The proposed IGU configuration integrates a laminated glazing system consisting of two standard clear glass panes (23 cm × 23 cm) enclosing 3% HGM along with an array of encapsulated monocrystalline silicon solar cells (15 cm × 15 cm). The *I*–*V* plot in Fig. 10a demonstrates a temperature-dependent PV performance enhancement of the IGU in comparison to a standalone Si-PV. At 20 °C, the IGU exhibits a modest increase in current density and voltage output relative to the standalone PV, indicating the successful integration and functional contribution of the HGM layer. As the temperature rises to 40 °C and 60 °C, the short-circuit current density (J_{SC}) significantly increases from approximately 17 mA cm^{-2} to over 22 mA cm^{-2}, while a slight reduction in open-circuit voltage (V_{OC}) is observed, an expected behaviour due to thermal voltage losses. This improved performance is attributed to thermally enhanced charge carrier mobility, lower internal resistance, and improved interfacial conductivity within the IGU structure. Correspondingly, the power conversion efficiency (PCE) increases from 6.4% at 20 °C to 7.38% at 40 °C, and further to 7.52% at 60 °C, reflecting a ~15% improvement over the standalone Si-PV. Table 2 highlights a comparative summary of the performance. Notably, the presence of HGM not only avoids optical

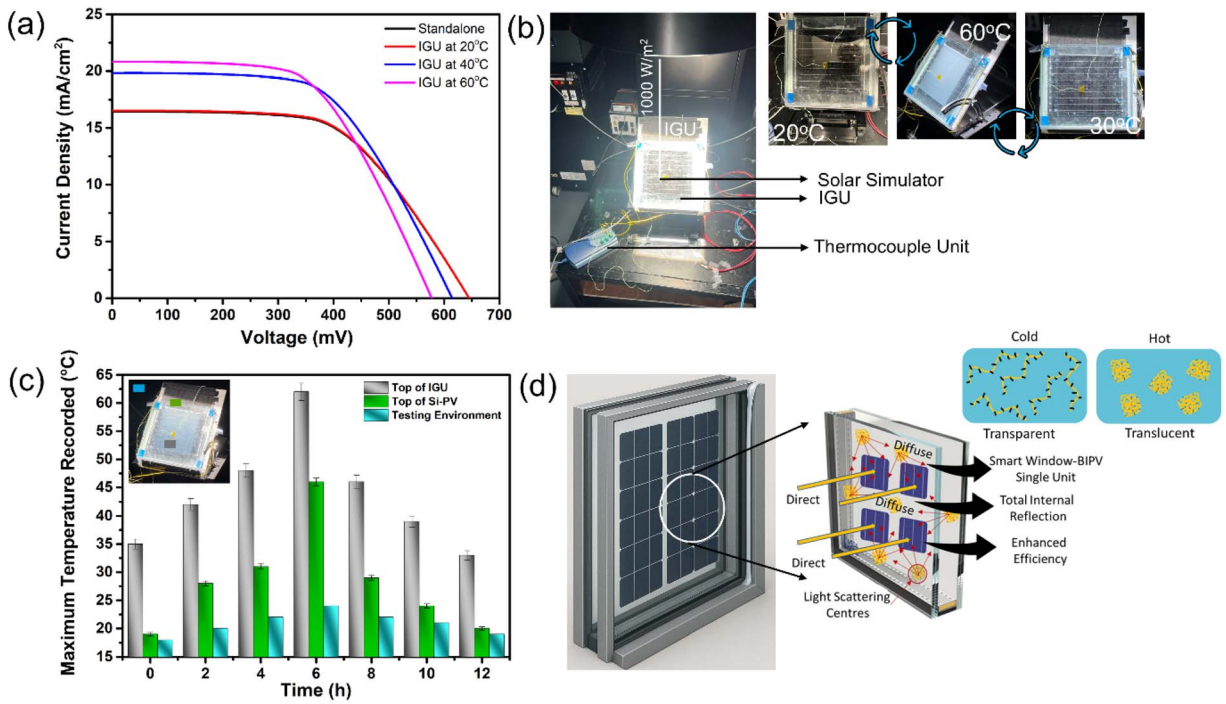

Fig. 10 (a) Current–voltage (*I*–*V*) characteristics of the IGU unit measured at different temperatures, (b) corresponding real-time optical images captured during testing, reflecting cyclic operation and dynamic response under varying thermal states, (c) temperature profile recorded over a continuous 12 hour testing period, demonstrating thermal stability and sustained device behaviour, (d) schematic representation of the proposed mechanism underlying the enhanced IGU performance at elevated temperatures.

Table 2 Comparative summary of the PV metrics of the 3% HGM IGU device compared with the standalone Si-PV

Device	J_{SC} (mA cm^{-2}) ± 0.5	V_{OC} (mV)	FF	PCE (%) ± 0.2
Si-PV	16.47	643	0.61	6.45
Si-PV + HGM = IGU	16.44	643	0.61	6.42
IGU at 40 °C	19.78	621	0.59	7.38
IGU at 60 °C	22.02	572	0.57	7.56

shading but actively contributes to performance enhancement under elevated temperatures, making the IGU a promising solution for thermally adaptive PV applications.

Furthermore, digital images captured at different time points during PV testing reveal changes in optical transparency and the evolution of light-scattering centres within the IGU, as shown in Fig. 10b. These visual changes correlate with temperature-dependent behaviour, suggesting dynamic modulation of the hydrogel matrix, which contributes to light diffusion and potentially enhances photon harvesting. Fig. 10c exhibits the temperature profile measurements recorded in parallel with the PV performance tests over a continuous 12-hour period using embedded thermocouples. Interestingly, the presence of HGM significantly reduces the surface temperature of the Si-PV layer by nearly half compared to the ambient temperature on the outer IGU glass surface. This temperature moderation effect is consistently observed throughout the day, with a minor but stable trend pattern. These findings confirm that the IGU not only maintains its operational stability under thermal stress but also enhances overall efficiency by regulating internal temperatures. Together, the results reinforce the IGU's potential as a thermally adaptive energy-harvesting system, capable of improving photovoltaic performance under real-world conditions.[60]

Further, the schematic in Fig. 10d illustrates how the thermo-responsive hydrogel interlayer within the IGU becomes an active light-management system at elevated temperatures. At low (ambient) temperatures the 3% HGM network is essentially molecularly dissolved and the IGU remains highly transparent, so direct solar irradiance passes through the glass and strikes the Si cells with minimal scattering (cold/transparent panel). As the temperature rises above the HGM's LCST (~30 °C), the hydrogel domains collapse into micron-scale polymer-rich "scattering centres" (hot/translucent panel). These microdomains act as Mie-scatterers, converting some of the normally transmitted direct beam into diffuse light within the IGU cavity.[29] The newly generated diffuse component undergoes multiple internal reflections and waveguiding between the glass panes, effectively increasing the optical path length across the silicon cell surfaces. This enhanced light trapping and angular redistribution boosts the photocurrent and overall PCE of the IGU, without significant parasitic absorption or shading losses.[27,61] In essence, the heat-activated phase separation of the hydrogel creates a dynamic, self-regulating light-scattering medium that amplifies PV performance under high-temperature operation.

3.9 Raman spectra and effect of shading

Raman spectroscopy of 3% HGM reveals strong cellulose–starch interactions during membrane formation, leading to an amorphous structure with labile bonds and scattering centers at 60 °C, as shown in Fig. 11a. The HGM exhibits multiple polymeric intensity bands in the 500–2000 cm^{-1} range, primarily attributed to the C–OH, C–O–C, and C–H vibrational modes of cellulose and starch. Key Raman peaks for cellulose include C–H stretching (~2910–2800 cm^{-1}), C–O–C stretching (~1150–1120 cm^{-1}, β-1,4-glycosidic linkage), C–O/C–C stretching (~1095–1080 cm^{-1}), and skeletal modes (~520–400 cm^{-1}, *e.g.*, ~380 cm^{-1} for crystalline cellulose Iβ). For starch, prominent peaks include C–H stretching (~2910–2850 cm^{-1}), C–O–C stretching (~940 cm^{-1}, α-1,4-linkage), C–O–C deformation (~860–850 cm^{-1}, α-1,6-branching), and a strong skeletal mode (~480 cm^{-1}). During membrane formation, these peaks undergo significant changes, indicating strong intermolecular interactions and structural reorganization.

At 60 °C, notable spectral changes were observed, particularly in the green-circled regions of Fig. 10a. The starch-associated peak at ~480 cm^{-1}, linked to glucose ring vibrations, nearly disappeared, suggesting a loss of crystalline order

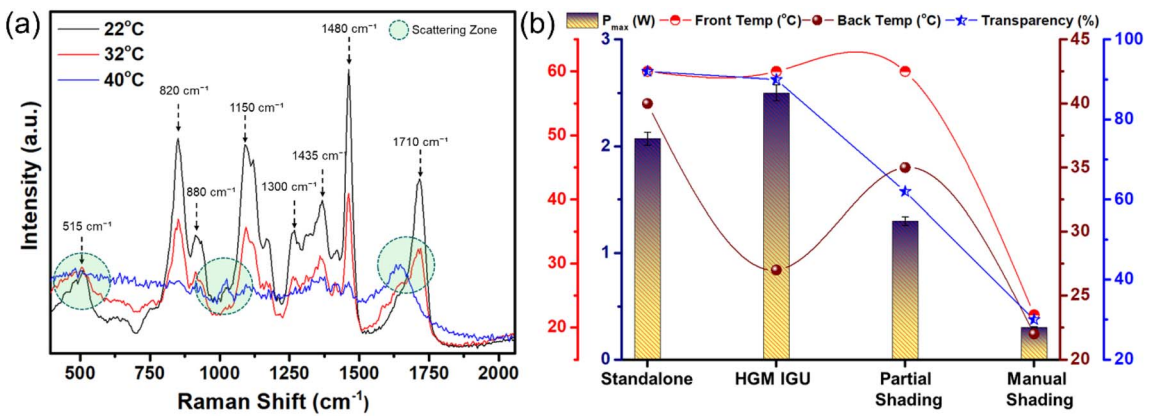

Fig. 11 (a) Temperature-dependent Raman spectra for the 3% HGM, and (b) the shading effect on the IGU's power output performance in terms of their relevant operating temperatures.

in starch's structure. Concurrently, a new peak emerged at ~1021 cm^{-1}, potentially indicating the formation of new C–O or C–C vibrational modes due to cellulose–starch interactions. An anti-Stokes shift was observed at ~1751 cm^{-1}, accompanied by significant peak broadening, particularly for C–H stretching (~2910–2800 cm^{-1}) and O–H stretching bands. This broadening is attributed to increased vibrational motion of cellulose and starch chains at higher temperatures, leading to overlapping vibrational modes and a more amorphous structure. The weakening of cellulose's crystalline peak (~380 cm^{-1}) and starch's ~940 cm^{-1} peak further supports the transition to an amorphous state, capturing labile H-bonds that enhance polymer chain flexibility.

These spectral changes suggest that the strong interaction between cellulose's β-1,4-linked linear chains and starch's α-1,4- and α-1,6-linked branched structure disrupts their native crystalline arrangements. The formation of scattering centres within the hydrogel matrix is primarily attributed to phase transitions from crystalline to amorphous states, as well as the presence of disordered polymer networks. The transition from an ordered crystalline structure to an amorphous configuration introduces regions with differing refractive indices, which disrupt the uniform transmission of light. Additionally, the inherent structural irregularities in the polymer network, such as chain entanglements, heterogeneous crosslinking densities, and microphase separation, further contribute to optical inhomogeneity. These factors collectively enhance light scattering within the material, thereby increasing its overall translucency.[62]

Consequently, due to the thermotropic properties of hydrogels, these materials can dynamically modulate light transmission, thereby introducing a self-adjusting shading effect on PV systems. This shading behaviour mimics the function of adaptive shading devices, such as Venetian blinds, which are traditionally employed to reduce glare and manage solar irradiance.[60] As shown in Fig. 11b, the influence of temperature-responsive hydrogel shading on PV cell performance was evaluated across varying levels of transparency, in comparison to conventional manual shading. Commercial Si-PV cells typically exhibit a negative temperature coefficient (−0.4 to −0.5% per °C), meaning that as cell temperature rises, V_{OC} decreases, fill factor declines, and overall conversion efficiency deteriorates. Moreover, partial shading of a PV module introduces a localized current mismatch, potential hot-spot formation, and power loss beyond the mere reduction of incident irradiance. The developed IGU addresses both phenomena by dynamically modulating light transmittance and managing thermal load. At ambient irradiance levels, the HGM remains highly transparent, permitting unimpeded photon flux into the silicon absorber. As cell temperature exceeds the phase-transition threshold (~35–40 °C), the HGM transitions to a translucent state which scatters incoming light rather than fully blocking it. This scattering effect redistributes photons toward the module's central active area, where carrier collection efficiency is maximized, thereby minimizing the localized current mismatch and reducing the risk of hot-spot formation. Simultaneously, the HGM attenuates infrared absorption at the glass–air interface, lowering back-surface temperature and mitigating thermalization losses that would otherwise depress V_{OC} and J_{SC}. In comparative experiments, modules equipped with HGM IGUs exhibited only a modest decline in optical transmittance (~60%) relative to the standalone Si PV yet achieved higher maximum power (P_{max}) due to stabilized cell temperature and enhanced photon harvesting. Consequently, this functioning underscores a paradigm shift in solar module design, where adaptive light management and localized heat dissipation collectively counteract conventional shading losses, enabling improved photovoltaic efficiency under thermally dynamic conditions.

3.10 Glazing transmission properties

Two key optical parameters, namely luminous transmission (T_{lum}) and solar transmission (T_{sol}), of the 3% HGM prototype window were quantitatively determined using eqn (2) and (3), respectively. These metrics are pivotal for evaluating the visual transparency and thermal performance of glazing systems. Specifically, T_{lum} denotes the fraction of incident visible light (typically within the 400–700 nm wavelength range) transmitted through the glazing material, while T_{sol} represents the overall proportion of incident solar radiation transmitted, encompassing the UV-vis-NIR spectral regions. The characterization

Table 3 Comparative study of luminous transmission and solar modulation of different hydrogels

Hydrogel sample type	Luminous transmission (%)	Solar modulation (%)	Transition temperature (°C)	Ref.
PNIPAM + SDS/PTH micelles	91	~76	29–36	61
PNIPAM/HPMC hydrogel	90.8	81.5	~32	64
Pure physical-crosslinked thermochromic hydrogel	92.7	82.1	Adjustable	65
Zwitterionic UCST hydrogel	37.1	Not specified	43	66
PNIPAM–AEMA hydrogel microparticles	87.2	81.3	~32	20
PNIPAM + AMEO crosslinker	96.8	89.7	33	67
Hybrid hydrogel with metal nanoparticles	~50–60	~20–30	—	68
PNIPAM-based printable thermochromic ink	—	—	32	69
HPC–PAA hydrogel – starch membrane form	~72	~78	~32	This work

was performed on the 3% HGM sample and the results were subsequently compared with relevant data reported in the extant literature as shown in Table 3.[63]

$$\text{Luminous transmission or reflection } T_{\text{lum}} = \frac{\sum_{\lambda=380\ \text{nm}}^{780\ \text{nm}} y(\lambda)T(\lambda)\Delta\lambda}{\sum_{\lambda=380\ \text{nm}}^{780\ \text{nm}} y(\lambda)\Delta\lambda} \quad (2)$$

$$\text{Solar transmission } T_{\text{sol}} = \frac{\sum_{\lambda=200\ \text{nm}}^{2000\ \text{nm}} \text{AM1.5}(\lambda)T(\lambda,\alpha)\Delta\lambda}{\sum_{\lambda=200\ \text{nm}}^{2000\ \text{nm}} \text{AM1.5}(\lambda)\Delta\lambda} \quad (3)$$

where $T(\lambda)$ is the transmittance of the composite coated at wavelength λ, the CIE (International Commission on Illumination) standards for photopic luminous efficiency of the human eye ($y(\lambda)$) and the solar irradiance spectrum for an air mass of 1.5 (AM1.5(λ)) were used as weighting functions for the wavelength-dependent transmittance. T_{lum} is 380 nm $\leq \lambda \leq$ 780 nm, corresponding to human vision limits. Besides, measurements were carried out at 510 nm compared to the CIE photopic luminous human eye efficiency. It should be noted that the transmission spectra results presented in this study are averaged values of at least five repeated experiments.

4. Conclusions

This study demonstrates the successful development of a transparent, biocompatible hydrogel membrane (HGM) synthesized from HPC and PAA, reinforced with starch derived from waste potato peels, exemplifying a sustainable approach through bio-waste valorization. The optimized 3% starch added HGM exhibits thermotropic behaviour, allowing dynamic modulation of optical transparency in response to temperature variations. Various physico-chemical analyses confirmed a stable and well-defined crosslinked polymer network that remains dynamic and responsive to temperature variations, underpinning the membrane's thermotropic behaviour and its ability to modulate optical and thermal properties effectively. Integration of the HGM into a prototype double-glazed window resulted in significant improvements in thermal regulation, achieving a low thermal conductivity of 0.23 W m^{-1} K^{-1} and a thermal transmittance (U-value) of 1.84 W m^{-2} K^{-1} calculated by a prototype hot–cold box method, effectively reducing temperature differentials by up to 30 °C. The membrane also demonstrated a tunable phase transition temperature, high luminous transmittance (~72%), notable solar modulation efficiency (75%), and excellent durability under operational conditions. One promising advantage of the smart window technology developed in this study is its potential for retrofitting existing windows. The HGM-incorporating window, characterized by its exceptional visible light transmission and significant solar modulation ability, holds broad applicability in the modern built environment. Importantly, incorporation of the HGM enhanced the performance of the underlying silicon photovoltaic cells by up to 15%, which is attributed to the presence of light-scattering centres within the hydrogel matrix that promote total internal reflection and mitigate local heating. Serving as both a passive cooling medium and an optical modulator, this hydrogel membrane offers dual functionality, making it a promising candidate for BIPV applications. Overall, this work advances energy-efficient and climate-adaptive architectural design by merging sustainable material development with improved solar and thermal management capabilities.

Data availability

The data supporting the findings of this study are available from the corresponding author upon reasonable request.

Author contributions

Anurag Roy: conceptualization, data curation, investigation, project administration, methodology, writing – original draft. Adeel Arshad: formal analysis, methodology, data curation, writing – review & editing. Tapas Kumar Mallick: supervision, resources, writing – review & editing. Asif Ali Tahir: supervision, validation, funding acquisition, writing – review & editing.

Conflicts of interest

There are no conflicts to declare.

Acknowledgements

The research described in this article was supported by the Engineering and Physical Sciences Research Council (EPSRC) in the UK, under research grant number EP/T025875/1. However, the EPSRC did not participate directly in the writing of this article. The authors also acknowledge Arthur Graf from the Harwell XPS Centre, Rutherford Appleton Laboratory, Didcot, UK, for his extensive support with the hydrogel's and HGM's cryo-XPS testing. Additionally, the authors express their gratitude to Dr Gavyn Rollinson, Experimental Officer and Technical Operations Manager at Camborne School of Mines, University of Exeter, Penryn Campus, Cornwall for his valuable assistance with SEM measurements of HGM samples. The authors acknowledge Mohammad Hadi Mohammadi, Research and Commercial Manager at the Critical Minerals Equipment Hub (CMEH), University of Exeter, Penryn Campus, Cornwall for his support with ATR-FTIR spectroscopy analysis for HGM samples.

References

1 M. González-Torres, *et al.*, A review on buildings energy information: Trends, end-uses, fuels and drivers, *Energy Rep.*, 2022, **8**, 626–637.
2 J. Min, *et al.*, The effect of carbon dioxide emissions on the building energy efficiency, *Fuel*, 2022, **326**, 124842.
3 M. W. Akram, *et al.*, Global technological advancement and challenges of glazed window, facade system and vertical

greenery-based energy savings in buildings: A comprehensive review, *Energy Built Environ.*, 2023, **4**(2), 206–226.
4 A. Ghosh, *et al.*, Active smart switchable glazing for smart city: A review, *J. Build. Eng.*, 2024, **84**, 108644.
5 Y. J. Hwang, *et al.*, Multi-stimuli-responsive and Multi-functional Smart Windows, *ChemNanoMat*, 2022, **8**(5), e202200005.
6 Z. Zhang, *et al.*, Thermochromic Energy Efficient Windows: Fundamentals, Recent Advances, and Perspectives, *Chem. Rev.*, 2023, **123**(11), 7025–7080.
7 D. Wang, G. Chen and J. Fu, Multifunctional thermochromic smart windows for building energy saving, *J. Mater. Chem. A*, 2024, **12**(22), 12960–12982.
8 T. Jiang, *et al.*, Dynamically adaptive window design with thermo-responsive hydrogel for energy efficiency, *Appl. Energy*, 2021, **287**, 116573.
9 R. Kundu, *et al.*, Cellulose hydrogels: Green and sustainable soft biomaterials, *Curr. Res. Green Sustainable Chem.*, 2022, **5**, 100252.
10 M. Leng and Y. Long, A smart way to wrap a building, *Nat Sustainability*, 2023, **6**(6), 619–620.
11 C. Zhao, Z. Ma and X. X. Zhu, Rational design of thermoresponsive polymers in aqueous solutions: A thermodynamics map, *Prog. Polym. Sci.*, 2019, **90**, 269–291.
12 V. S. Raghuwanshi and G. Garnier, Characterisation of hydrogels: Linking the nano to the microscale, *Adv. Colloid Interface Sci.*, 2019, **274**, 102044.
13 Y. Zhou, *et al.*, Hydrogel smart windows, *J. Mater. Chem. A*, 2020, **8**(20), 10007–10025.
14 K. Ryu, *et al.*, Thermoresponsive Hydrogels for the Construction of Smart Windows, Sensors, and Actuators, *Acc. Mater. Res.*, 2025, **6**(3), 379–392.
15 K. Wang, *et al.*, Hofmeister Effect-Enhanced, Nanoparticle-Shielded, Thermally Stable Hydrogels for Anti-UV, Fast-Response, and All-Day-Modulated Smart Windows, *Adv. Mater.*, 2025, **37**(14), 2418372.
16 J. M. Dodda, *et al.*, Hydrogels: Definition, History, Classifications, Formation, Constitutive Characteristics, and Applications, in *Multicomponent Hydrogels: Smart Materials for Biomedical Applications*, ed. J. M. Dodda, K. Deshmukh and D. Bezuidenhout, The Royal Society of Chemistry, 2023.
17 Y. Zhou, *et al.*, Unconventional smart windows: Materials, structures and designs, *Nano Energy*, 2021, **90**, 106613.
18 C. Zhang, *et al.*, Hydrogel-Based Functional Materials for Thermoelectric Applications: Progress and Perspectives, *Adv. Funct. Mater.*, 2024, **34**(51), 2410127.
19 Y. Zhou, *et al.*, Liquid Thermo-Responsive Smart Window Derived from Hydrogel, *Joule*, 2020, **4**(11), 2458–2474.
20 X.-H. Li, *et al.*, Broadband Light Management with Thermochromic Hydrogel Microparticles for Smart Windows, *Joule*, 2019, **3**(1), 290–302.
21 Q. Lei, *et al.*, Active-passive dual-control smart window with thermochromic synergistic fluidic glass for building energy efficiency, *Build. Environ.*, 2022, **222**, 109407.
22 Y. Chen and C. Zheng, Physically Cross-Linked Hydrogel Designed for Thermochromic Smart Windows: Balance between Thermal Stability and Processability, *ACS Sustain. Chem. Eng.*, 2025, **13**(6), 2574–2585.
23 H. Yuk, *et al.*, Tough bonding of hydrogels to diverse non-porous surfaces, *Nat. Mater.*, 2016, **15**(2), 190–196.
24 X. Hu, *et al.*, Weak Hydrogen Bonding Enables Hard, Strong, Tough, and Elastic Hydrogels, *Adv. Mater.*, 2015, **27**(43), 6899–6905.
25 Y. Ding, *et al.*, Multiple Stimuli-Responsive Cellulose Hydrogels with Tunable LCST and UCST as Smart Windows, *ACS Appl. Polym. Mater.*, 2020, **2**(8), 3259–3266.
26 J. R. McKee, *et al.*, Thermoresponsive Nanocellulose Hydrogels with Tunable Mechanical Properties, *ACS Macro Lett.*, 2014, **3**(3), 266–270.
27 N. M. Mohammad, *et al.*, Highly Tunable Cellulosic Hydrogels with Dynamic Solar Modulation for Energy-Efficient Windows, *Small*, 2024, **20**(27), 2303706.
28 Y. Guo, *et al.*, Hydrogels and Hydrogel-Derived Materials for Energy and Water Sustainability, *Chem. Rev.*, 2020, **120**(15), 7642–7707.
29 X. Liu and Y. Wu, Experimental characterisation of a smart glazing with tuneable transparency, light scattering ability and electricity generation function, *Appl. Energy*, 2021, **303**, 117521.
30 F. Ebrahimian, J. F. M. Denayer and K. Karimi, Potato peel waste biorefinery for the sustainable production of biofuels, bioplastics, and biosorbents, *Bioresour. Technol.*, 2022, **360**, 127609.
31 S. Khanal, *et al.*, Sustainable utilization and valorization of potato waste: state of the art, challenges, and perspectives, *Biomass Convers. Biorefin.*, 2024, **14**(19), 23335–23360.
32 S. M. Ali, *et al.*, Extraction and characterization of starch from low-grade potatoes and formulation of gluten-free cookies containing modified potato starch, *Heliyon*, 2023, **9**(9), e19581.
33 A. Roy, T. K. Mallick and A. A. Tahir, An optimal climate-adaptable hydrogel-filled smart window for the energy-saving built environment, *J. Mater. Chem. C*, 2022, **10**(41), 15474–15482.
34 A. Arshad, *et al.*, Shape-Stabilized PEGylated Silica Aerogel-Composite as an Energy Saving Building Material, *Ind. Eng. Chem. Res.*, 2023, **62**(47), 20236–20250.
35 M. M. R. Al-Fartoos, *et al.*, A semi-transparent thermoelectric glazing nanogenerator with aluminium doped zinc oxide and copper iodide thin films, *Commun. Eng.*, 2024, **3**(1), 145.
36 A. Roy, *et al.*, Certified high-efficiency "large-area" perovskite solar module for Fresnel lens-based concentrated photovoltaics, *iScience*, 2023, **26**(3), 106079.
37 E. Abraham, *et al.*, Highly transparent silanized cellulose aerogels for boosting energy efficiency of glazing in buildings, *Nat. Energy*, 2023, **8**(4), 381–396.
38 V. A. Maiorov, Optical Properties of Thermotropic Hydrogels (a Review), *Opt. Spectrosc.*, 2020, **128**(3), 367–386.
39 K. Li, *et al.*, Durable and Controllable Smart Windows Based on Thermochromic Hydrogels, *ACS Appl. Mater. Interfaces*, 2020, **12**(37), 42193–42201.

40 D. G. Prajapati and B. Kandasubramanian, A Review on Polymeric-Based Phase Change Material for Thermo-Regulating Fabric Application, *Polym. Rev.*, 2020, **60**(3), 389–419.
41 W. Wang and S. A. Sande, A dynamic light scattering study of hydrogels with the addition of surfactant: a discussion of mesh size and correlation length, *Polym. J.*, 2015, **47**(4), 302–310.
42 J. Zhang, *et al.*, Static and dynamic experiments on hydrogels: Effects of the chemical composition of the fluid, *Mech. Mater.*, 2021, **154**, 103717.
43 S. Wang, *et al.*, Design and fabrication of functional hydrogels with specific surface wettability, *Colloid Interface Sci. Commun.*, 2023, **52**, 100697.
44 M. T. Rauter, S. K. Schnell and S. Kjelstrup, Cassie–Baxter and Wenzel States and the Effect of Interfaces on Transport Properties across Membranes, *J. Phys. Chem. B*, 2021, **125**(46), 12730–12740.
45 F. Wang, *et al.*, Design Principles and Emerging Applications of Starch-Involved Superwettable Systems, *Engineering*, 2025, DOI: 10.1016/j.eng.2025.04.022.
46 P. M. Fechner, *et al.*, Influence of Water on Molecular and Morphological Structure of Various Starches and Starch Derivatives, *Starch*, 2005, **57**(12), 605–615.
47 R. Foudazi, *et al.*, Porous Hydrogels: Present Challenges and Future Opportunities, *Langmuir*, 2023, **39**(6), 2092–2111.
48 J. Shrivastava and A. K. Bajpai, Starch-based hydrogels, in *Plant and Algal Hydrogels for Drug Delivery and Regenerative Medicine*, ed. T. K. Giri and B. Ghosh, Woodhead Publishing, 2021, ch. 3, pp. 75–112.
49 R. Soni, T.-A. Asoh and H. Uyama, Cellulose nanofiber reinforced starch membrane with high mechanical strength and durability in water, *Carbohydr. Polym.*, 2020, **238**, 116203.
50 P. A. I. Sponchiado, *et al.*, Biomembranes Based on Potato Starch Modified by Dry Heating Treatment: One Sustainable Strategy to Amplify the Use of Starch as a Biomaterial, *Biomacromolecules*, 2025, **26**(3), 1530–1540.
51 W. Xu, M. Jia and Z. Gong, Thermal conductivity and tortuosity of porous composites considering percolation of porous network: From spherical to polyhedral pores, *Compos. Sci. Technol.*, 2018, **167**, 134–140.
52 A. Duda, Z. Koza and M. Matyka, Hydraulic tortuosity in arbitrary porous media flow, *Phys. Rev. E: Stat., Nonlinear, Soft Matter Phys.*, 2011, **84**(3), 036319.
53 A. Hemaida, *et al.*, Evaluation of thermal performance for a smart switchable adaptive polymer dispersed liquid crystal (PDLC) glazing, *Sol. Energy*, 2020, **195**, 185–193.
54 L. Gao, *et al.*, Synergistic Effect of Hydrogen Bonds and Chemical Bonds to Construct a Starch-Based Water-Absorbing/Retaining Hydrogel Composite Reinforced with Cellulose and Poly(ethylene glycol), *ACS Omega*, 2021, **6**(50), 35039–35049.
55 J. Tian, *et al.*, Mechanically robust multifunctional starch films reinforced by surface-tailored nanofibrillated cellulose, *Composites, Part B*, 2024, **275**, 111339.
56 F. Zhou, *et al.*, The filling effects of starch-based emulsion microgels in gel-based systems, *Food Biosci.*, 2024, **57**, 103608.
57 Z. Yang, H. Yang and H. Yang, Effects of sucrose addition on the rheology and microstructure of κ-carrageenan gel, *Food Hydrocolloids*, 2018, **75**, 164–173.
58 H. Nasution, *et al.*, Hydrogel and Effects of Crosslinking Agent on Cellulose-Based Hydrogels: A Review, *Gels*, 2022, **8**(9), 568.
59 P.-H. Elchinger, D. Montplaisir and R. Zerrouki, Starch–cellulose crosslinking—Towards a new material, *Carbohydr. Polym.*, 2012, **87**(2), 1886–1890.
60 Q. Wang, *et al.*, Smart Photovoltaic Windows for Next-Generation Energy-Saving Buildings, *Adv. Sci.*, 2024, **11**(44), 2407177.
61 Z. Yu, *et al.*, Bidirectional optical response hydrogel with adjustable human comfort temperature for smart windows, *Mater. Horiz.*, 2024, **11**(1), 207–216.
62 L. Svenningsson and L. Nordstierna, Polarized Raman Spectroscopy Strategy for Molecular Orientation of Polymeric Fibers with Raman Tensors Deviating from the Molecular Frame, *ACS Appl. Polym. Mater.*, 2020, **2**(11), 4809–4813.
63 A. Roy, *et al.*, Synergistic Effect of Paraffin-Incorporated In_2O_3/ZnO Multifold Smart Glazing Composite for the Self-Cleaning and Energy-Saving Built Environment, *ACS Sustain. Chem. Eng.*, 2022, **10**(20), 6609–6621.
64 K. Wang, *et al.*, Thermo-Responsive Poly(N-isopropylacrylamide)/Hydroxypropylmethyl Cellulose Hydrogel with High Luminous Transmittance and Solar Modulation for Smart Windows, *ACS Appl. Mater. Interfaces*, 2023, **15**(3), 4385–4397.
65 W. Gao, *et al.*, Pure Physical-Crosslinked High-Strength Thermochromic Hydrogel for Smart Window and Energy Conservation, *Adv. Funct. Mater.*, 2025, **35**(16), 2418941.
66 J. Chen, *et al.*, Zwitterionic hydrogel smart windows: Radiative cooling, privacy protection and energy savings, *Nano Energy*, 2024, **123**, 109386.
67 G. Zhu, *et al.*, Thermochromic Smart Windows with Ultra-High Solar Modulation and Ultra-Fast Responsive Speed Based on Solid–Liquid Switchable Hydrogels, *Research*, 2024, **7**, 0462.
68 Y. Wang, *et al.*, Metal nanoparticle hybrid hydrogels: the state-of-the-art of combining hard and soft materials to promote wound healing, *Theranostics*, 2024, **14**(4), 1534–1560.
69 G. Chen, *et al.*, Printable Thermochromic Hydrogel-Based Smart Window for All-Weather Building Temperature Regulation in Diverse Climates, *Adv. Mater.*, 2023, **35**(20), 2211716.

